

Design and Generation of Stochastically Defined, Pulsed FM Noise Waveforms

Charles A. Mohr and Shannon D. Blunt

Radar Systems Lab (RSL), University of Kansas, Lawrence, KS

Abstract—The design and physical generation of diverse radar emissions often requires optimization of unique waveforms on an individual basis. Consequently, a significant processing overhead is incurred that could make real-time implementation impractical. To address this limitation, families of pulsed FM noise waveforms are defined here according to a parameterized process denoted as Stochastic Waveform Generation (StoWGe). Through the use of expectation metrics and an expected frequency template error (EFTE) cost function a particular waveform family is specified via a desired spectral shape so that each physical FM waveform can be easily produced by drawing samples from a random process. Performance is assessed via simulation and experimentally in loopback and open-air testing.

Keywords—FM noise waveforms, waveform optimization, waveform diversity

I. INTRODUCTION

Waveform diversity remains a topic of significant interest for a variety of radar modalities [1]. A prominent topic within this area for quite some time has been that of noise radar [2–5] due to its low probability of intercept (LPI) characteristics, though the inherent requirement of amplitude modulation (AM) tends to limit utility to short-range applications and precludes the use of high-power amplifiers (HPAs). More recently, the notion of FM noise radar has begun to emerge which, while not really LPI, is amenable to high-power, and thus long-range, applications.

The theoretical attributes of FM noise radar were first examined by Axelsson [6] and recently furthered by Pralon, et al [7, 8]. Various approaches for the implementation and optimization of FM noise waveforms have also been experimentally demonstrated [9–12], leading to a host a new capabilities including different forms of radar-embedded communications [13, 14], nonlinear harmonic radar [15], simultaneous dual-polarized emissions [16], practical implementation of complementary FM waveforms [17], and practical spectral notching on transmit [18].

In general, these optimization approaches have operated on individual waveforms. Consequently, achieving true waveform agility in which each pulse is modulated by a unique, non-repeated waveform can incur a hefty computational burden within the transmitter, to the point where it may simply be more reasonable to optimize and store a set of waveforms ahead of time. Of course, growing demands on spectral congestion and the associated need for environmentally responsive waveforms [19] may likewise limit a storage-based approach.

To address the computational bottleneck of real-time waveform design and generation we consider a perspective in which the waveform phase function is defined according to an explicitly parameterized stochastic process. By subsequently expressing the (otherwise deterministic) waveform metrics of autocorrelation and spectral density in stochastic terms, a parameterizing structure can be optimized

such that independent instantiations of a random process produce an entire family of random FM waveforms that can be directly implemented in a high-power transmitter.

II. EVALUATING STOCHASTIC WAVEFORMS

First consider a discrete pulsed waveform representation defined according to a discrete-time random process as

$$s[m] = \begin{cases} \exp(j\phi[m]) & m = 1, 2, \dots, M \\ 0 & \text{otherwise} \end{cases} \quad (1)$$

where the member functions of $s[m]$ are individual, pulsed waveforms and $\phi[m]$ is itself a random process. For now, we make no assumptions about $\phi[m]$ other than that it is real valued (spectral containment is addressed later). The form of (1) can be written more succinctly as the length M vector

$$\mathbf{s} = \exp(j\phi). \quad (2)$$

It is likewise convenient to define the vector

$$\bar{\mathbf{s}} = [\mathbf{s}^T \mathbf{0}_{W-M}^T]^T \quad (3)$$

for $W \geq 2M - 1$ so that the discrete Fourier transform (DFT) of (3) can be written as

$$\mathbf{s}_f = \mathbf{A} \bar{\mathbf{s}}, \quad (4)$$

where \mathbf{A} is the $W \times W$ DFT matrix.

Based on this representation the expected power spectral density (PSD) over a given family of waveforms is

$$E[|\mathbf{s}_f|^2], \quad (5)$$

where $E[\cdot]$ is element-wise expectation and $|\cdot|^2$ is element-wise magnitude-squared. Thus we would anticipate that the sample-mean PSD for a finite set of waveforms belonging to the same family to approach (5) as the number of waveforms grows large. For example, in some applications one could reasonably expect a coherent processing interval (CPI) to be comprised of hundreds to thousands of pulsed waveforms.

In addition to the aggregate characteristics represented by (5) it is important to understand how random waveforms perform on an individual basis. Consequently

$$E[|\mathbf{s}_f|^4] - E[|\mathbf{s}_f|^2]^2 \quad (6)$$

measures the expected deviation from (5) in a mean-square sense. That is, if (5) has a desirable form, it would be advantageous to minimize (6) such that the individual waveform PSDs resemble the expected PSD as closely as possible. Of course, there could alternatively be situations in which greater per-waveform diversity is desired.

The expected integrated autocorrelation can be expressed via the inverse DFT (IDFT) of (5) as

$$\mathbf{A}^H E[|\mathbf{s}_f|^2], \quad (7)$$

which represents the aggregate autocorrelation one would obtain after coherently integrating over an infinite number of

match-filtered waveforms. The per-waveform expected autocorrelation can likewise be determined by computing the root mean-square (RMS) response as

$$\left(E \left[\left| \mathbf{A}^H \mathbf{s}_f \right|^2 \right] \right)^{1/2}. \quad (8)$$

Now expand the expected PSD from (5) as

$$E[|\mathbf{s}_f|^2] = E[\mathbf{A} \bar{\mathbf{s}} \odot (\mathbf{A} \bar{\mathbf{s}})^*], \quad (9)$$

for \odot the Hadamard product and $(\cdot)^*$ denoting complex conjugation. Representing the matrix multiplications in summation form and by linearity of the expectation operator, (9) can then be rewritten in the per-sample form

$$E[|\mathbf{s}_{f,w}|^2] = \sum_{m_1=1}^W \sum_{m_2=1}^W a_{w,m_1} a_{w,m_2}^* E[\bar{s}_{m_1} \bar{s}_{m_2}^*] \quad (10)$$

where a_{ij} is the ij th element of matrix \mathbf{A} . The fourth-order component of (6) can likewise be written in the per-sample form

$$E[|\mathbf{s}_{f,w}|^4] = \sum_{m_1=1}^W \sum_{m_2=1}^W \sum_{m_3=1}^W \sum_{m_4=1}^W a_{w,m_1} a_{w,m_2} a_{w,m_3}^* a_{w,m_4}^* E[\bar{s}_{m_1} \bar{s}_{m_2} \bar{s}_{m_3}^* \bar{s}_{m_4}^*]. \quad (11)$$

The important terms in (10) and (11) are

$$E[\bar{s}_{m_1} \bar{s}_{m_2}^*] \quad (12)$$

and

$$E[\bar{s}_{m_1} \bar{s}_{m_2} \bar{s}_{m_3}^* \bar{s}_{m_4}^*] \quad (13)$$

that represent the second-order and fourth-order moments for particular samples of $\bar{\mathbf{s}}$, respectively. These terms can be collected into the structures $\bar{\mathbf{C}}_{W \times W}$ and $\bar{\mathbf{K}}_{W \times W \times W \times W}$, where $\bar{\mathbf{C}}$ is a correlation matrix and $\bar{\mathbf{K}}$ is a fourth-order moment hyper-cube. Note that $\bar{\mathbf{C}}$ and $\bar{\mathbf{K}}$ also include the moments of the zero-valued elements of $\bar{\mathbf{s}}$, so the non-zero portions are simply $\mathbf{C}_{M \times M}$ and $\mathbf{K}_{M \times M \times M \times M}$.

III. STOCHASTIC FM WAVEFORM MODEL

Returning to the simple discrete-time waveform representation of (2), we now explicitly specify the phase such that it conforms to

$$\phi = \mathbf{B}\mathbf{x} + \boldsymbol{\mu}. \quad (14)$$

Here \mathbf{B} is an $M \times N$ matrix of basis functions similar to the forms in [11, 17, 20] that are generalizations of polyphase-coded FM (PCFM) [21], \mathbf{x} is a length- M vector of real-valued, statistically independent Gaussian random variables distributed on $\mathcal{N}(0,1)$, and $\boldsymbol{\mu}$ is a length- M vector of constants corresponding to the expected value of ϕ (needed to produce an asymmetric spectrum). In contrast to previous parameterized FM waveform optimization approaches [11, 17, 20-22] in which \mathbf{x} contains the set of parameters to optimize, here it is the matrix \mathbf{B} and vector $\boldsymbol{\mu}$ that comprise the structure being designed.

By taking advantage of the properties of Gaussian distributions, similar to the steps taken in [6], and based on the fact that each term in \mathbf{x} is statistically independent, the distribution of the m th element in ϕ is

$$\phi_m \sim \mathcal{N}(\mu_m, \mathbf{b}_m \mathbf{b}_m^T) \quad (15)$$

in which \mathbf{b}_m is the m th row of matrix \mathbf{B} and the product $\mathbf{b}_m \mathbf{b}_m^T$ is a scalar. Noting that (12) can be rewritten as

$$E[\bar{s}_{m_1} \bar{s}_{m_2}^*] = E[\exp(j(\phi_{m_1} - \phi_{m_2}))] \quad (16)$$

due to (1), for $m_1, m_2 \leq M$, it then follows based on (15) that

$$\phi_{m_1} - \phi_{m_2} \sim \mathcal{N}(\mu_{m_1} - \mu_{m_2}, (\mathbf{b}_{m_1} - \mathbf{b}_{m_2})(\mathbf{b}_{m_1} - \mathbf{b}_{m_2})^T). \quad (17)$$

Likewise, (13) can be rewritten as

$$E[\bar{s}_{m_1} \bar{s}_{m_2} \bar{s}_{m_3}^* \bar{s}_{m_4}^*] = E[\exp(j(\phi_{m_1} + \phi_{m_2} - \phi_{m_3} - \phi_{m_4}))] \quad (18)$$

where

$$\begin{aligned} &(\phi_{m_1} + \phi_{m_2} - \phi_{m_3} - \phi_{m_4}) \\ &\sim \mathcal{N}(\mu_{m_1} + \mu_{m_2} - \mu_{m_3} - \mu_{m_4}, \\ &(\mathbf{b}_{m_1} + \mathbf{b}_{m_2} - \mathbf{b}_{m_3} - \mathbf{b}_{m_4})(\mathbf{b}_{m_1} + \mathbf{b}_{m_2} - \mathbf{b}_{m_3} - \mathbf{b}_{m_4})^T) \end{aligned} \quad (19)$$

for $m_1, m_2, m_3, m_4 \leq M$.

Recognizing that the right-hand side of (16) takes the form of the characteristic function, and exploiting the fact that the characteristic function of a Gaussian random variable is also Gaussian, (12) ultimately becomes

$$\begin{aligned} &E[\bar{s}_{m_1} \bar{s}_{m_2}^*] \\ &= \exp(j(\mu_{m_1} - \mu_{m_2}) - 0.5(\mathbf{b}_{m_1} - \mathbf{b}_{m_2})(\mathbf{b}_{m_1} - \mathbf{b}_{m_2})^T). \end{aligned} \quad (20)$$

Since the right-hand side of (18) also has this same general form, (13) therefore becomes

$$\begin{aligned} &E[\bar{s}_{m_1} \bar{s}_{m_2} \bar{s}_{m_3}^* \bar{s}_{m_4}^*] \\ &= \exp(j(\mu_{m_1} + \mu_{m_2} - \mu_{m_3} - \mu_{m_4}) - \\ &0.5(\mathbf{b}_{m_1} + \mathbf{b}_{m_2} - \mathbf{b}_{m_3} - \mathbf{b}_{m_4})(\mathbf{b}_{m_1} + \mathbf{b}_{m_2} - \mathbf{b}_{m_3} - \mathbf{b}_{m_4})^T). \end{aligned} \quad (21)$$

Using (20) and (21), it is thus possible to compute (5)-(8) in closed form once \mathbf{B} and $\boldsymbol{\mu}$ are determined.

IV. EXPECTED FREQUENCY TEMPLATE ERROR

Consider the design of a family of random waveforms such that the expected PSD in (5) matches a desired template. Optimizing individual FM waveforms according to a frequency template error (FTE) metric was previously investigated in [11, 22]. Here a stochastic version, denoted as expected FTE (EFTE), is defined as

$$J = \left\| E[|\mathbf{s}_f|^2] - \mathbf{u} \right\|_2^2, \quad (22)$$

where \mathbf{u} is the $W \times 1$ desired spectral template and $\|\cdot\|_2^2$ is the squared 2-norm.

Minimizing (22) as a function of \mathbf{B} and $\boldsymbol{\mu}$ enables the expected PSD to be a good approximation of the desired spectrum \mathbf{u} for random instantiations of \mathbf{x} . Theoretically, a Gaussian power spectrum corresponds to a Gaussian autocorrelation, which is sidelobe-free by definition. Since a Gaussian spectrum has the added benefit of providing good spectral containment, it is an obvious choice for \mathbf{u} . That said, this approach is applicable to arbitrary PSD shapes and could possibly be particularly useful to generate random waveforms containing spectral notches [18].

A. Gradient-Based Optimization of \mathbf{B} and $\boldsymbol{\mu}$

Due to the non-convexity of (22), minimization necessitates the use of approximate methods. As shown in

[11, 17, 20, 23, 24], gradient-descent methods are effective at minimizing this kind of cost function. Specifically, for \mathbf{q}_k the current set of parameters and \mathbf{p}_k the current descent direction, the update is performed via

$$\mathbf{q}_{k+1} = \mathbf{q}_k + \alpha_k \mathbf{p}_k \quad (23)$$

where α_k is the current step-size. Here the descent direction is determined according to

$$\mathbf{p}_k = \begin{cases} -\mathbf{g}_0 & \text{when } k = 0 \\ -\mathbf{g}_k + \beta \mathbf{p}_{k-1} & \text{otherwise} \end{cases} \quad (24)$$

in which β depends on the particular form of gradient-descent employed and \mathbf{g}_k is the current gradient.

Denoting $b_{\ell,n}$ as the term in the ℓ th row and n th column of \mathbf{B} and μ_r as the r th element of $\boldsymbol{\mu}$, the derivative of (22) with respect to each of these values is

$$\frac{\partial J}{\partial b_{\ell,n}} = 2 \left[\frac{\partial E[|\mathbf{s}_f|^2]}{\partial b_{\ell,n}} \right]^T (E[|\mathbf{s}_f|^2] - \mathbf{u}) \quad (25)$$

and

$$\frac{\partial J}{\partial \mu_r} = 2 \left[\frac{\partial E[|\mathbf{s}_f|^2]}{\partial \mu_r} \right]^T (E[|\mathbf{s}_f|^2] - \mathbf{u}). \quad (26)$$

The partial derivatives with respect to \mathbf{s}_f in (25) and (26) are taken element-wise, which for the w th element of \mathbf{s}_f is

$$\frac{\partial E[|\mathbf{s}_{f,w}|^2]}{\partial b_{\ell,n}} = \sum_{m=1}^M 2 \Re \{ a_{w,\ell} a_{w,m}^* c_{\ell,m} (b_{\ell,n} - b_{m,n}) \} \quad (27)$$

and

$$\frac{\partial E[|\mathbf{s}_{f,w}|^2]}{\partial \mu_r} = \sum_{m=1}^M 2 \Im \{ a_{w,r}^* a_{w,m} c_{\ell,m} \} \quad (28)$$

respectively. The term $c_{\ell,m}$ is the element in the ℓ th row and m th column of matrix \mathbf{C} , and the operations $\Re\{\cdot\}$ and $\Im\{\cdot\}$ extract the real and imaginary parts of the argument.

By iteratively calculating these values within the gradient-descent framework above, (22) can be minimized to obtain \mathbf{B} and $\boldsymbol{\mu}$ with which to generate the associated family of random FM waveforms. Further, (20) and (21) can be computed to subsequently obtain (5)-(8).

V. ANALYSIS OF STOCHASTIC WAVEFORM GENERATION

Consider the optimization of an $M \times N$ matrix \mathbf{B} and a length M vector $\boldsymbol{\mu}$ to achieve a family of random StoWGe waveforms in which the expected PSD is Gaussian. The value of N , which also corresponds to the waveform time-bandwidth product BT , is set to 150 (for B the 3-dB bandwidth). The value of M is set to 900, which corresponds to an over-sampling factor of 6 relative to the 3-dB bandwidth. This relatively high value for over-sampling was chosen to illustrate the spectral roll-off region, which is quite important to consider for physical waveforms.

The initial form of \mathbf{B} used here for gradient-descent optimization was inspired by the simple basis functions that arise for the first-order PCFM implementation [21]. Thus the columns of \mathbf{B} initially consist of time-shifted ramp functions, where the ramp portion comprises six samples that are preceded by zeros and followed by ones. The vector $\boldsymbol{\mu}$ was

initialized with zeros and the desired template \mathbf{u} is a discretized Gaussian shape, likewise with appropriate over-sampling. The optimization process was allowed to run for 10,000 iterations.

A. StoWGe Basis Function Characteristics

A consequence of initializing $\boldsymbol{\mu}$ with all zeroes and \mathbf{u} having a symmetric spectrum is that $\boldsymbol{\mu}$ remains unchanged after optimization and all the correlation parameters are real-valued. For this family of StoWGe waveforms the matrix \mathbf{B} is therefore solely responsible for generating each particular random waveform given a random instantiation of \mathbf{x} .

Figure 1 illustrates four of the 150 different, length-900 basis functions in \mathbf{B} . Aside from a delay shift, the orange and yellow basis functions in the center are effectively identical. In contrast, the blue and purple basis functions near the respective ends of the pulse are somewhat different due to their proximity to the pulse edges. It has been observed (for this desired PSD) that the basis functions comprising roughly the first and last 15% of the pulse change according to the respective pulse edge, while the remaining basis functions throughout the middle of the pulse are identical aside from the delay shift. Note that the basis functions all have a smooth response, which is a result of the good spectral containment of the Gaussian PSD and the inclusion of sufficient spectral roll-off. Further, aside from those near the edge, each basis function still starts at zero and ends at one just like the PCFM initialization.

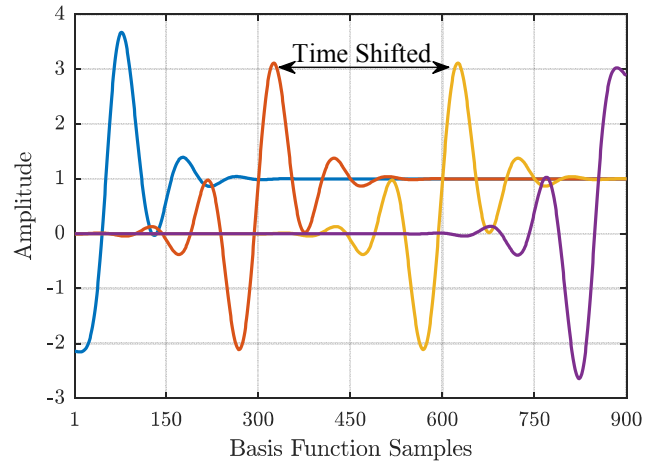


Fig. 1. Representative StoWGe basis functions from matrix \mathbf{B} when optimizing for a Gaussian PSD

The rapid rise/fall of the pulse edges, which corresponds to broader frequency content than the waveform modulation in this case, impacts the optimization of \mathbf{B} and $\boldsymbol{\mu}$, and consequently the correlation matrix \mathbf{C} . This effect can be partly visualized by plotting the magnitudes of the values of \mathbf{C} as shown in Fig. 2 for the upper-left corner of the matrix, which pertains to the region at/near the leading edge of the pulse. After sample index 6, notable for also being the over-sampling factor, a Toeplitz form can be observed. In contrast, sample indices 1-5 display changing characteristics that may be an emergent phenomena that is attempting to compensate, to the degree actually possible, for the extended spectral content of the rapid rising edge so that the desired spectral containment can be achieved. The same effect occurs at the falling edge of the pulse.

Finally, Fig. 3 illustrates the instantaneous frequency as a function of time for a few random FM waveforms belonging to this StoWGe family. In general, the instantaneous frequency of the different waveforms stays within the 3-dB bandwidth of $\pm B/2$, as indicated by the dashed black lines, and when it does exceed the 3-dB bandwidth, it does so only briefly. Of particular note is the more rapid oscillation of instantaneous frequency at the beginning and end of each pulse that can be observed in the inset of Fig. 3. This behavior is directly attributable to the different basis functions near the pulse edges as discussed above.

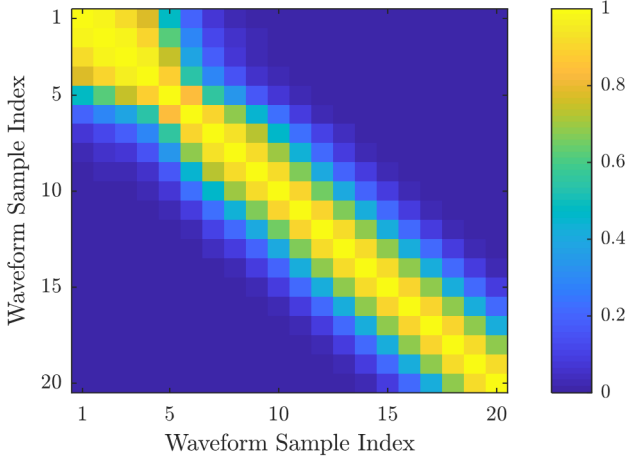


Fig. 2. Top-left 20 × 20 section of correlation matrix \mathbf{C}

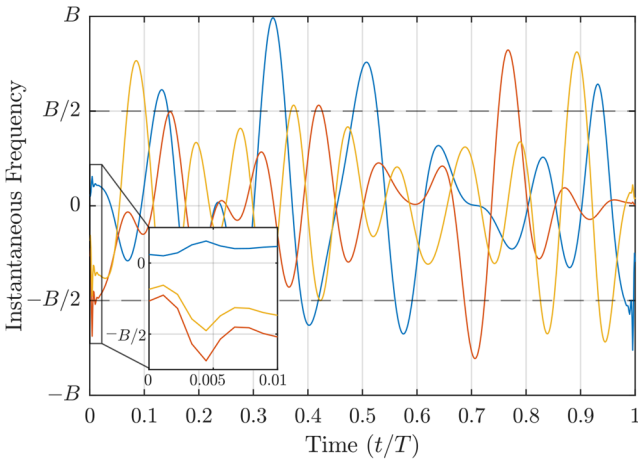


Fig. 3. Instantaneous frequency over the pulsewidth for a few example StoWGe waveforms

B. StoWGe Waveform Performance

To evaluate the practical performance of these stochastic waveforms the optimized \mathbf{B} and $\boldsymbol{\mu}$ obtained above were used to generate 3000 random waveforms using (14) via independent instantiations of \mathbf{x} . Coherent integration of the resulting 3000 autocorrelation responses provides a sample mean to compare with the analytical coherent response of (7). Likewise, RMS combining of the 3000 autocorrelation responses serves as a comparison for the analytical RMS response of (8). For the given \mathbf{B} and $\boldsymbol{\mu}$, the moments in \mathbf{C} and \mathbf{K} can be calculated and thus so can (10) and (11), which facilitates direct computation of (7) and (8).

Figure 4 shows that the sample RMS result (dark blue trace) computed over the 3000 waveforms is in near-perfect agreement with the analytical RMS (dashed orange trace) computed from (8). Moreover, these results show a per-

formance waveform peak sidelobe level (PSL) of just better than -21 dB, which agrees with the anticipated $-10\log_{10}(BT) = -21.8$ dB when $BT = 150$.

The coherent traces, on the other hand, exhibit a notable difference. The sample coherent result (light blue trace in Fig. 4) obtained from coherently integrating the 3000 unique autocorrelations (the same procedure as slow-time Doppler processing) reveals a PSL of -52 dB, which itself agrees fairly well with the additional $10\log_{10}(3000) = 34.8$ dB reduction relative to the -21.8 dB RMS result (totaling -56.6 dB) that one would anticipate from the incoherent combining of random sidelobes. In contrast, the analytical coherent result (red trace) computed using (7) depicts only the mainlobe because the sidelobe level resides at MATLAB's numerical precision limit of -300 dB. While such a value is meaningless in a real system, the result clearly implies that, if one could hypothetically combine the autocorrelations from an infinite number of waveforms from this family in a coherent manner, the sidelobes would become nonexistent. This result likewise agrees with the lack of autocorrelation sidelobes one would expect for a Gaussian PSD. Further, it can be deduced from this analytical result that increasing the number of unique StoWGe waveforms in the CPI will continue to decrease the resulting sidelobes after pulse compression and Doppler processing, such as has been observed when random waveforms were optimized individually [9-18].

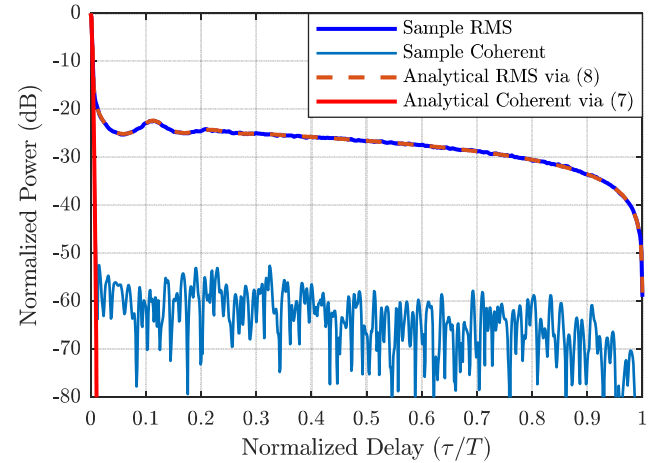


Fig. 4. Comparison of sample-mean and analytical versions of the RMS and coherent autocorrelation responses of StoWGe waveforms (Gaussian PSD)

Figure 5 then illustrates how the sample-mean PSD (blue trace) computed over 3000 StoWGe waveforms relates to the analytical expected PSD (orange trace) from (5) and the desired Gaussian spectral template \mathbf{u} . The sample-mean and analytical versions clearly match quite well, though both deviate from the template at about -35 dB and encounter a floor at -40 dB. This spectral floor was also previously observed in [11] and corresponds to the spectral containment that can feasibly be achieved due to the (theoretically instantaneous) rise/fall-time of the pulse. As demonstrated in [25], it may become necessary to modify the transmitter architecture for high-power systems in order to “slow down” this sharp rise/fall-time in practice if further improvement in spectral containment is required.

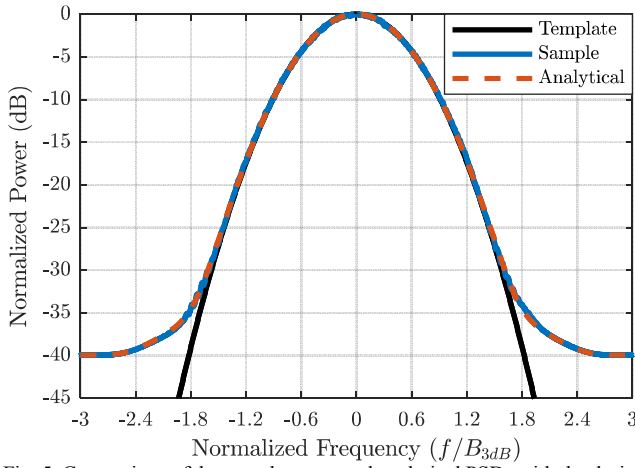


Fig. 5. Comparison of the sample-mean and analytical PSDs with the desired Gaussian template

VI. EXPERIMENTAL RESULTS

To verify the analytic results above and to assess the physical robustness of StoWGe waveforms within a radar transmitter, the waveforms from the previous section were implemented on hardware in both a loopback configuration and in open-air tests.

A. Loopback Assessment

For hardware implementation, the 200 MSample/sec sample rate baseband waveforms were up-sampled to 10 GSamples/sec and digitally unconverted to a center frequency of 3.55 GHz. The waveforms from the previous section were then implemented on a Tektronix AWG70002A arbitrary waveform generator (AWG) and passed through a class A amplifier followed by an attenuator and a low noise amplifier (LNA) to emulate some of the transmitter effects. The signals were then captured on a Rhode & Schwarz FSW real-time spectrum analyzer (RSA) that is serving as the receiver.

Figure 6 shows the RMS power spectrum of the 3000 waveforms implemented in loopback along with the expected PSD spectrum computed via (5) and the desired spectral template. Figure 7 likewise depicts the RMS autocorrelation and the coherently integrated (summed) autocorrelation of the same experimentally implemented waveforms against their analytically calculated counterparts computed via (8) and (7), respectively.

In Fig. 6 the effect of the RSA anti-aliasing filter is apparent from the steep spectral roll-off beyond about $|f| \leq 2.4$ in normalized frequency. Otherwise, the experimental RMS power spectrum closely matches the analytically calculated expected spectrum (just like Fig. 5). Likewise in Fig. 7, the experimental RMS autocorrelation is virtually identical to its simulated (Fig. 4) and analytically calculated counterparts.

B. Open-Air Measurements

Finally, the set of StoWGe waveforms was transmitted in an open-air scenario using the same generation and recording equipment as employed for loopback capture. Using separate transmit and receive antennas in a pseudo-monostatic configuration on the roof of Nichols Hall on the University of Kansas campus, the responses from moving target traversing the intersection of 23rd and Iowa Streets in Lawrence, KS were obtained.

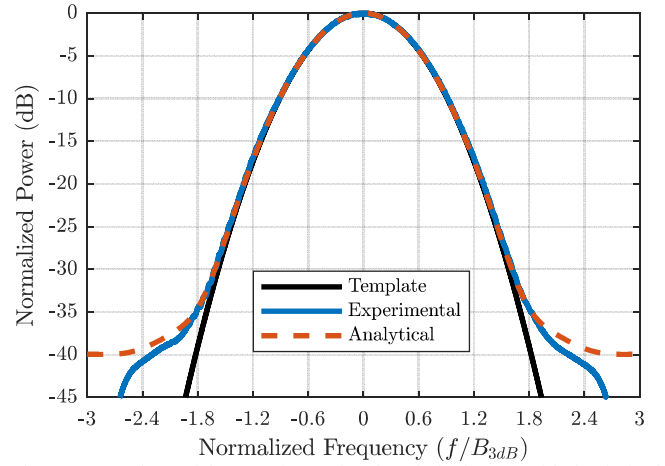


Fig. 6. Comparison of the experimental and analytical PSDs with the desired Gaussian template

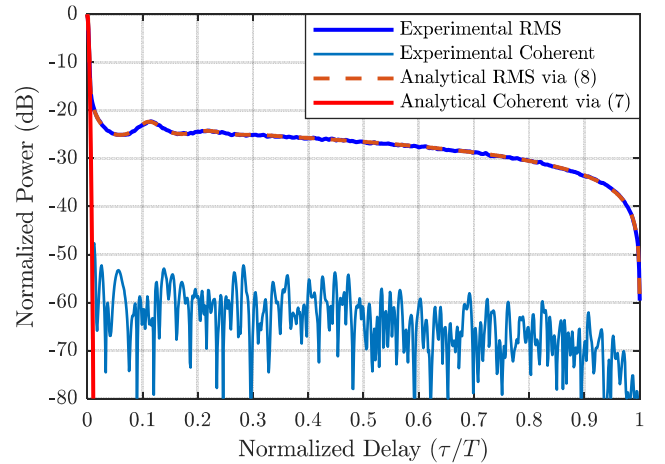


Fig. 7. Comparison of the experimental and analytical versions of the RMS and coherent autocorrelation responses

Figure 8 shows the measured range profile in which several discrete scatterers are visible, including the direct path (between transmit and receive antennas), a tree line at ~ 150 m, some structures on the KU campus at ~ 600 m, and illuminated intersection of interest. The nominal level of the coherently integrated sidelobes can be observed in the convolutional tail of the direct path to the left of 0 m to be about -55 dB, which agrees with the coherent trace in Fig. 7.

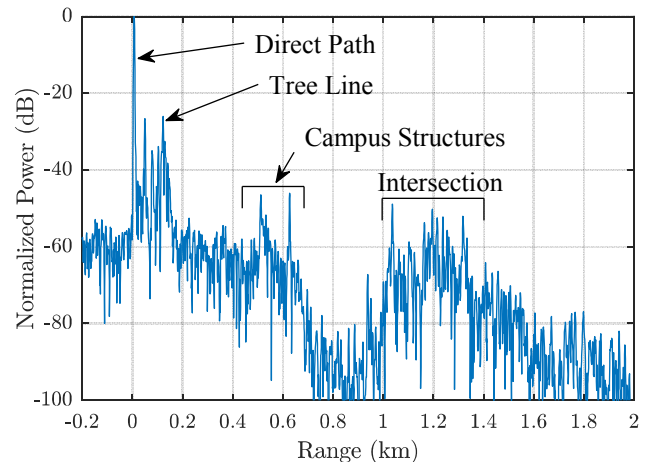


Fig. 8. Open-air measured range profile using 3000 StoWGe waveforms after matched filtering and slow-time coherent integration

To assess the utility of StoWGe waveforms for moving target indication (MTI), a range-Doppler plot was formed (Fig. 9) in the vicinity of the intersection at ~1100 m. Due to the stationary platform a simple projection-based clutter notch was used along with a Hamming window to suppress Doppler sidelobes. Various moving vehicles are easily visible. Thus the StoWGe formulation represents an easy way in which to produce useful and physically realizable random FM waveforms.

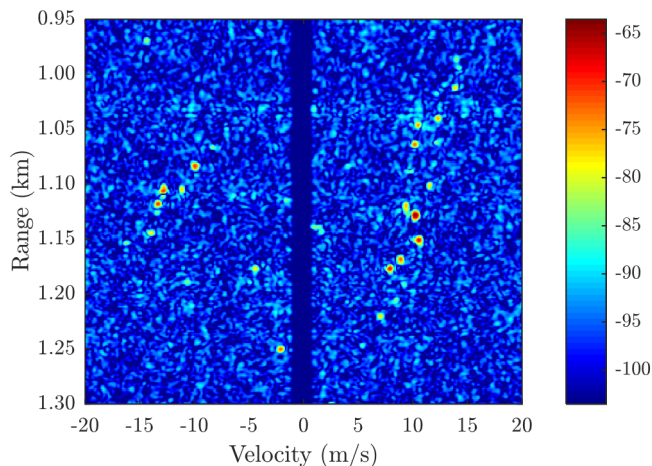


Fig. 9. Open-air measured range-Doppler response produced using StoWGe waveforms

VII. CONCLUSIONS

A stochastic formulation to generate families of random FM waveforms has been derived according to a desired PSD. By optimizing a parameterized structure comprised of basis functions and expected phase values (the latter to address asymmetric spectra), unique waveforms from a given Stochastic Waveform Generation (StoWGe) family can be readily obtained from independent sets of Gaussian random variables (the terms in \mathbf{x}). The performance of these random waveforms was evaluated analytically and also experimentally in both loopback and open-air testing.

REFERENCES

- [1] S.D. Blunt, E.L. Mokole, "An overview of radar waveform diversity," *IEEE AESS Systems Magazine*, vol. 31, no. 11, pp. 2-42, Nov. 2016.
- [2] B.M. Horton, "Noise-modulated distance measuring systems," *Proc. IRE*, vol. 47, no. 5, pp. 821-828, May 1959.
- [3] X. Xu, R.M. Narayanan, "Range sidelobe suppression technique for coherent ultra wide-band random noise radar imaging," *IEEE Trans. Antennas & Propagation*, vol. 49, no. 12, pp. 1836-1842, Dec. 2001.
- [4] D. Tarchi, K. Lukin, J. Fortuny-Guasch, A. Mogyla, P. Vyplavin, A. Sieber, "SAR imaging with noise radar," *IEEE Trans. Aerospace & Electronic Systems*, vol. 46, no. 3, pp. 1214-1225, July 2010.
- [5] M. Malanowski, K. Kulpa, "Detection of moving targets with continuous-wave noise radar: theory and measurements," *IEEE Trans. Geoscience & Remote Sensing*, vol. 50, no. 9, pp. 3502-3509, Sept. 2012.
- [6] S.R.J. Axelsson, "Noise radar using random phase and frequency modulation," *IEEE Trans. Geoscience & Electronic Systems*, vol. 42, no. 11, pp. 2370-2384, Nov. 2004.
- [7] L. Pralon, B. Pompeo, J.M. Fortes, "Stochastic analysis of random frequency modulated waveforms for noise radar systems," *IEEE Trans. Aerospace & Electronic Systems*, vol. 51, no. 2, pp. 1447-1461, Apr. 2015.
- [8] L. Pralon, G. Beltrao, B. Pompeo, M. Pralon, J.M. Fortes, "Near-thumbtack ambiguity function of random frequency modulated signals," *IEEE Radar Conf.*, Seattle, WA, May 2017.
- [9] J. Jakabosky, S.D. Blunt, B. Himed, "Waveform design and receive processing for nonrecurrent nonlinear FMCW radar," *IEEE Intl. Radar Conf.*, Arlington, VA, May 2015.
- [10] J. Jakabosky, S.D. Blunt, B. Himed, "Spectral-shape optimized FM noise radar for pulse agility," *IEEE Radar Conf.*, Philadelphia, PA, May 2016.
- [11] C.A. Mohr, P.M. McCormick, S.D. Blunt, C. Mott, "Spectrally-efficient FM noise radar waveforms optimized in the logarithmic domain," *IEEE Radar Conf.*, Oklahoma City, OK, Apr. 2018.
- [12] C.A. Mohr, S.D. Blunt, "FM noise waveforms optimized according to a temporal template error (TTE) metric," *IEEE Radar Conf.*, Boston, MA, Apr. 2019.
- [13] C. Sahin, J. Jakabosky, P. McCormick, J. Metcalf, S. Blunt, "A novel approach for embedding communication symbols into physical radar waveforms," *IEEE Radar Conf.*, Seattle, WA, Apr. 2017.
- [14] B. Ravenscroft, P.M. McCormick, S.D. Blunt, E. Perrins, J.G. Metcalf, "A power efficient formulation of tandem-hopped radar & communications," *IEEE Radar Conf.*, Oklahoma City, OK, Apr. 2018.
- [15] J. Owen, C. Mohr, S.D. Blunt, K. Gallagher, "Nonlinear radar via intermodulation of jointly optimized FM noise waveform pairs," *IEEE Radar Conf.*, Boston, MA, Apr. 2019.
- [16] G. Zook, P.M. McCormick, S.D. Blunt, C. Allen, J. Jakabosky, "Dual-polarized FM noise radar," *IET Intl. Radar Conf.*, Belfast, UK, Oct. 2017.
- [17] C.A. Mohr, P.M. McCormick, S.D. Blunt, T. Higgins, "Complementary waveform subsets within an FM noise radar CPI," *IEEE Radar Conf.*, Oklahoma City, OK, Apr. 2018.
- [18] B. Ravenscroft, J.W. Owen, J. Jakabosky, S.D. Blunt, A.F. Martone, K.D. Sherbondy, "Experimental demonstration and analysis of cognitive spectrum sensing & notching," *IET Radar, Sonar & Navigation*, vol. 12, no. 12, pp. 1466-1475, Dec. 2018.
- [19] H. Griffiths, et al, "Radar spectrum engineering and management: technical and regulatory issues," *Proc. IEEE*, vol. 103, no. 1, pp. 85-102, Jan. 2015.
- [20] P.M. McCormick, S.D. Blunt, "Gradient-based coded-FM waveform design using Legendre polynomials," *IET Intl. Conf. Radar Systems*, Belfast, UK, Oct. 2017.
- [21] S.D. Blunt, M. Cook, J. Jakabosky, J.D. Graaf, E. Perrins, "Polyphase-coded FM (PCFM) radar waveforms, part I: implementation," *IEEE Trans. AES*, vol. 50, no. 3, pp. 2218-2229, July 2014.
- [22] S.D. Blunt, J. Jakabosky, M. Cook, J. Stiles, S. Seguin, E.L. Mokole, "Polyphase-coded FM (PCFM) radar waveforms, part II: optimization," *IEEE Trans. Aerospace & Electronic Systems*, vol. 50, no. 3, pp. 2230-2241, July 2014.
- [23] P.M. McCormick, S.D. Blunt, "Nonlinear conjugate gradient optimization of polyphase-coded FM radar waveforms," *IEEE Radar Conf.*, Seattle, WA, May 2017.
- [24] C.A. Mohr, S.D. Blunt, "Analytical spectrum representation for physical waveform optimization requiring extreme fidelity," *IEEE Radar Conf.*, Boston, MA, Apr. 2019.
- [25] L. Ryan, J. Jakabosky, S.D. Blunt, C. Allen, L. Cohen, "Optimizing polyphase-coded FM waveforms within a LINC transmit architecture," *IEEE Radar Conf.*, Cincinnati, OH, May 2014.